The Development and Characterization of Ultra High GIGA-Strength Ferritic Hot Band Steels

Bing Ma[1,2], Yingjie Wu[1], Mingjian Hua[1,3], Juha Uusitalo[4] and Anthony J. DeArdo[1,4*]

[1] Basic Metals Processing Research Institute, Department of Mechanical Engineering and Materials Science, Swanson School of Engineering, University of Pittsburgh, 636 Benedum Hall, 3700 O'Hara Street, Pittsburgh, PA, 15261, US.

[2] Global Solar Energy, Inc., 8500 S. Rita Rd, Tucson, AZ, 85747, US.

[3] Sichuan University – Pittsburgh Institute (SCUPI), Sichuan University, Zone 4, Liberal Arts Building, Jiang'an Campus, Chengdu, Sichuan Province 610207, China.

[4] Centre for Advanced Steels Research, Materials Engineering Laboratory, Department of Mechanical Engineering, University of Oulu, P.O Box 4200, FI-90014, Oulu, Finland.

ORCID numbers of all authors and the email address of corresponding author:

Bing Ma: 0000-0003-4842-4403;

Yingjie Wu: 0000-0002-7062-7568;

Mingjian Hua: 0000-0001-7539-8023;

Juha Uusitalo: 0000-0001-7393-6465;

Anthony J. DeArdo*: 0000-0003-3485-4496; deardo@pitt.edu

ABSTRACT

The correlations existing among the hot mill processing, as-coiled microstructure and mechanical properties of a Mo-Ti-V microalloyed hot rolled high strength steel were investigated in this current study. Discrete processing parameters, i.e., finish rolling temperatures (FRT) and coiling temperatures (CT), were applied and the corresponding microstructures and mechanical properties were analyzed. It was found that the FRT had only a very minor influence on either microstructures or mechanical properties. However, the CTs strongly affected both the microstructures and mechanical properties. The microstructure in the matrix was observed to change from mainly polygonal ferrite to quasi-polygonal ferrite to granular bainite and upper bainite with falling CTs, accompanied by the formation of martensite/austenite (M/A) constituents

at the lower CTs. The strength appeared to be increased by the dislocations originating by the shear component of the displacive phase transformation, and by fine (Ti, Mo)C precipitates, both formed during the coiling process. Strengths reaching values as high as 1166 MPa in yield strength and 1225 MPa in tensile strength were observed in specimens after coiling at 610°C, and the steels still had a reasonable total elongation of around 20%. However, the hole expansion ratios of these steel conditions were rather low in this study, especially for those with higher strength. Several factors appeared to contribute to the poor hole expansion ratios found in these steel conditions: the presence of coarse TiN inclusions, a large amount of strengthening precipitates and a high dislocation density as well as the presence of M/A constituents.

Keywords: Ferritic hot band steels, Thermo-mechanical controlled processing, Precipitation hardening, Dislocation strengthening, TiN inclusions, Hole expansion

1. Introduction

In mass reduction programs in the automotive industry to simultaneously improve fuel efficiency, lower CO_2 emissions, and strengthen the passenger crumble zone, the major focus has been the body-in-white (BIW), where the highest amount of steel sheet is used. To reduce this mass, thinner advanced high strength steels (AHSS) are being substituted for heavier gauge lower strength older steels. Compared with conventional high strength low alloy (HSLA) steels [1], the AHSS steels, generally with yield strengths (YS) easily exceeding 500 MPa, can offer much higher ultimate tensile strengths (UTS) in excess of 1000 MPa [2]. Moreover, successful candidate steels must also have adequate levels of global formability (total elongation), local formability (sheared edge ductility), and crumple zone resistance. However, popular candidate steels for the BIW include the new multi-phase AHSS: dual-phase (DP), transformation induced plasticity (TRIP), complex phase (CP) and martensitic (MART) steels, as these steels can exhibit high strength with reasonable global ductility but only limited local ductility [2–6].

Recently, a new generation of microalloyed hot band steels has been proposed and developed. The microstructural design of these steels was intended to combine high strength through ferrite grain size control and precipitation hardening[7–9], and high sheared edge ductility or hole expansion ratios (HER) by having a monolithic ferrite matrix phase since high HER values are often associated with spatially uniform matrix hardness [10,11]. A few examples have been made through this path as hot band coils with a gauge thickness from 3 to 4 mm through

conventional processing. Both of them involved precipitation strengthening with nano-sized precipitates containing Ti, Mo [12] or Mo, Nb, V [13,14] in a fine-grained ferritic matrix, and exhibited a high UTS and superior HER results.

In this present study, a similar experimental design philosophy, i.e. using a monolithic microstructure, was applied, and the goal was to produce a hot band steel with a YS larger than 1000 MPa and a UTS in excess of 1200 MPa, also with good ductility and hole expansion ratio. The effect of thermomechanical processing for ferrite grain refinement, and the presence of microalloying elements Mo, Ti and V for precipitation were studied in a 0.14 wt.% C - 1.35 Mn carbon steel. To alter the ferrite grain size and microstructures, the steels were produced with different finish rolling temperatures (FRT) and coiling temperatures (CT). The effect of processing parameters on the formation of microstructures was explored and the observed microstructures were correlated to the mechanical properties.

2. Experimental Procedure

The chemical composition of the steel investigated in this study is given in Table 1. The steel was laboratory vacuum melted then hot rolled to 3 mm in two stages. In the first stage, the ingots were reheated to 1200ºC and then rough hot rolled to 22 mm, followed by air cooling to room temperature (ACRT). In the second stage, the 22 mm slabs were further hot rolled to 3 mm, but with different FRTs, i.e., 870ºC, 810ºC and 750ºC. Immediately after hot rolling, the 3 mm thick steels were rapidly water spray cooled at about 30ºC s^{-1} to coiling temperatures of 610ºC, 530ºC and 450ºC, after which they were furnace cooled about 1 hour, followed by ACRT to room temperature. This TMCP used is shown schematically in Figure 1.

Table 1

Chemical composition (wt.%)

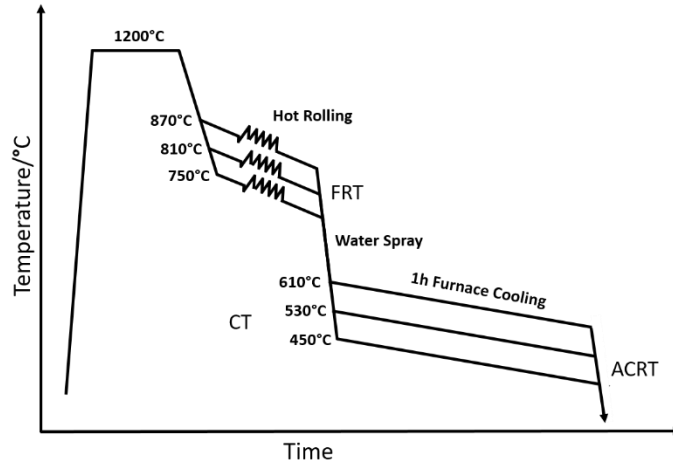| C	Si	S	P	Mn	Mo	V	Ti	N	S.Al	Nb
0.140	0.293	0.0034	0.011	1.370	0.350	0.294	0.163	0.006	0.049	0.002

Figure 1. The schematic illustration of the thermo-mechanical processing in this study

All steels were cut, mounted, ground and polished to make metallographic samples with a surface containing both rolling direction (RD) and normal direction (ND). The samples were etched with 2% Nital reagent for optical microscope (OM) and scanning electron microscope (SEM) observation. To identify martensite/austenite (M/A) constituent, re-polished samples were etched with alkaline sodium picrate and observed under OM. Electron backscattered diffraction (EBSD) was applied for the analysis of detailed crystallographic information. Carbon extraction replicas for transmission electron microscope (TEM) were prepared for the observation of fine precipitates.

Uniaxial room temperature tensile tests, conforming to ASTM E8, were performed on the sub-sized specimens with longitudinal direction along the rolling direction, at a strain rate of 1.1×10^{-3} s-1 with an Intron Microforce Testing System (MTS). In addition, hole expansion tests were conducted on the 100 mm $\times$ 100 mm hot band specimens at a speed of 0.3 cm min-1, according to ISO Standard TS 16630 Technical Specification for hole expansion testing [15,16]. A camera with adjustable lenses was installed to facilitate the observation of the process, the HER were calculated after the test finished, and the fracture surfaces were observed under SEM.

3. Results
3.1. Microstructures of the hot band coiled steels
3.1.1 Matrix behavior

Figure 2 shows the SEM micrographs imaged with secondary electrons and taken with a low magnification of hot band coil conditions after being etched by 2% Nital. In Figure 2, the steel condition sharing the same CTs seem to have similar microstructures, while the microstructures of steels with different CTs are distinctly different. Considering the final microstructures of the steel conditions with the CT of 610°C, shown in Figures 2 (a), (d) and (g) are a mixture of ferrite grains of varying shape, size and type, including what appears to be polygonal ferrite (PF), quasi-polygonal ferrite (QF) and acicular ferrite (AF). In terms of the lower temperature (i.e., 530°C or 450°C) coiled hot band steels, the ferrite grain boundaries become more irregular, and a second non-polygonal ferritic constituent (such as upper bainite (UB), granular bainite (GB) and M/A constituents) are also observed in Figures 2 (b), (c), (e), (f), (h) and (i).
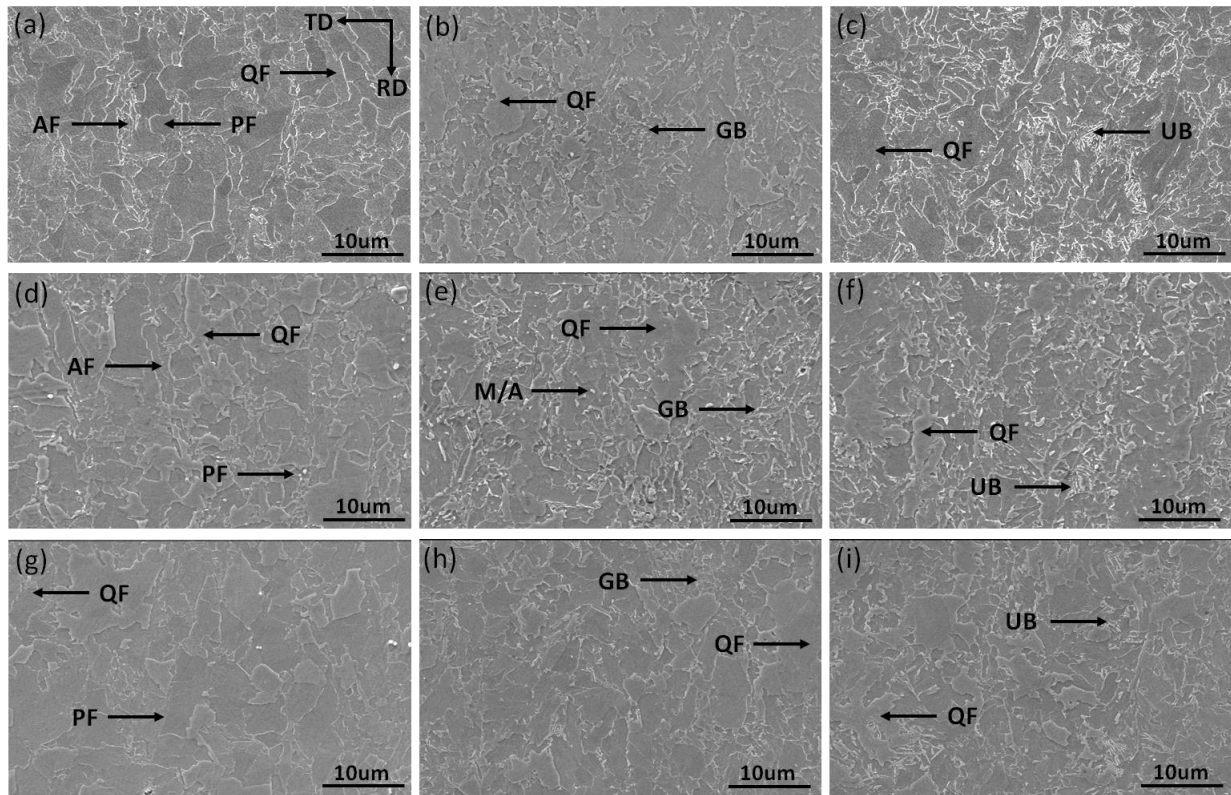

Figure 2. SEM micrographs of hot band coils at steel conditions of: (a) FRT:870°C/ CT:610°C, (b) 870°C/530°C, (c) 870°C/450°C, (d) 810°C/610°C, (e) 810°C/530°C, (f) 810°C/450°C, (g) 750°C/610°C, (h) 750°C/530°C and (i) 750°C/450°C. Imaging by secondary electron mode.

Figures 3 and 4 are SEM micrographs with different magnifications taken after being etched in 2% Nital reagent. The lowering of the CT results in the morphology change of the ferrite

grains, as well as the phase change within the ferrite. Figure 3 shows the SEM micrographs of hot band coils with a FRT of 810°C, but with varying coiling temperatures. Figure 3 (a) with a CT of 610°C, the specimen exhibits principally a mixed microstructure of polygonal and quasi-polygonal ferrite grains. In Figure 3 (b), the microstructure shows a mixture of mainly QF and GB where M/A constituents are observed dispersed within the ferrite grains or on the grain boundaries. Some of the M/A is located in the bainitic ferrite, i.e., GB, while some is randomly located in or near the QF. For the steel condition with a CT of 450°C, QF, UB and a small amount of martensite appear as shown in Figure 3 (c).
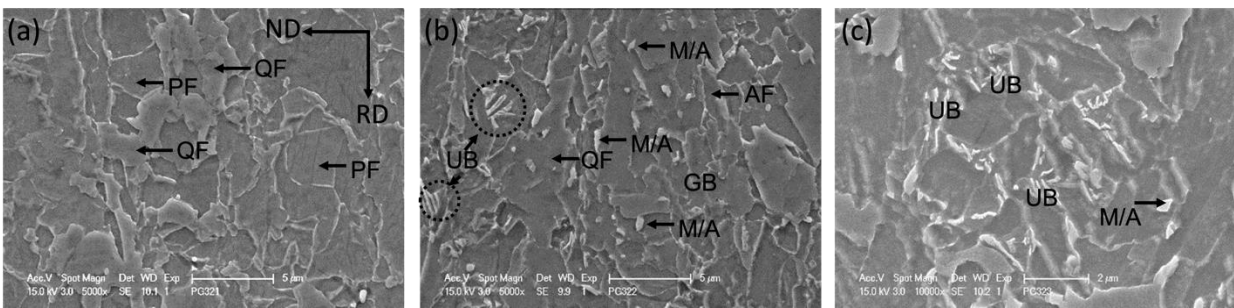

Figure 3. SEM micrographs of hot band coils at steel conditions of: (a) FRT:810°C/ CT:610°C, (b) 810°C/ 530°C and (c) 810°C/ 450°C.
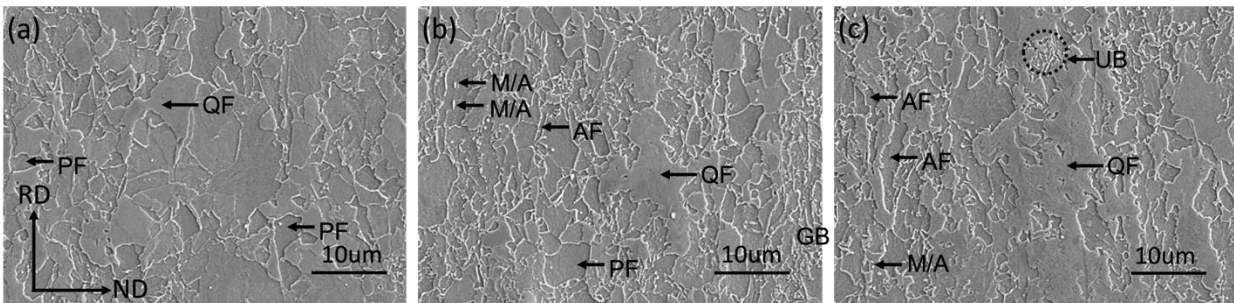

Figure 4. SEM micrographs of hot band coils at steel conditions of: (a) FRT:750°C/ CT:610°C, (b) 750°C/530°C and (c) 750°C/450°C.

Figure 4 shows the SEM micrographs taken of the hot band coils with a lower magnification. From Figures 4 (a) to 4 (c), when the FRT is 750°C, the SEM micrographs of the steel coiled at 610°C show mainly polygonal ferrite with a certain amount of acicular ferrite. However, as the coiling temperature drops to 530°C or 450°C, some coarse QF grains with irregular grain boundaries can be observed in the final microstructures.

Figures 5 to 7 are results generated from SEM-EBSD. Figure 5 shows the inverse pole figures (IPF) with high angle ferrite grain boundaries (HAGB) of all the steel conditions. The IPF illustrates the positions of the crystal coordinate system with respect to the sample coordinate system. The orientation triangle shown in Figure 5 (a) presents the orientation of the normal direction of the grains represented by different colors. It shows the steel conditions with a CT of 610°C have the most uniform grain sizes with a random distribution of grain crystallographic orientations. However, regarding the low temperature (i.e., 530°C or 450°C) coiled hot band steels, the coarse and elongated QF grains with a blue-purple crystallographic orientation can be clearly seen.

The kernel average misorientation (KAM) maps of all the steel conditions are presented in Figure 6. The KAM data was calculated using the 1st nearest neighbor kernel with a local misorientation threshold of 15°. It clearly shows a much higher percentage of sub-grain structures (green features) in the steel conditions with lower CTs. The dislocation density with the CT of 610°C showed a low but uniform level; however, it became lower and uneven at CTs of 530°C and 450°C, indicating mixed microstructures. It also draws the same conclusion that the FRT does not strongly affect the microstructure.

The grain boundary character distribution (GBCD) curves and misorientation curves from the EBSD results are exhibited in Figure 7. From the GBCD curves, it seems that all the steel conditions with the same coiling temperatures have similar results. With a CT of 610°C, there is a much larger fraction of high angle grain boundaries (HAGB) and a smaller fraction of low angle grain boundaries (LAGB), as expected from PF, than observed at lower coiling temperatures. Also, the fraction of coincidence site lattice (CSL, Σ3 to 29) grain boundaries does not vary very much. It is obvious that the difference in the GBCD is related to the transformation and microstructural changes that vary with transformation or coiling temperature. The GB misorientation distributions are presented in Figures 7 (d) to (f) for all the steel conditions.
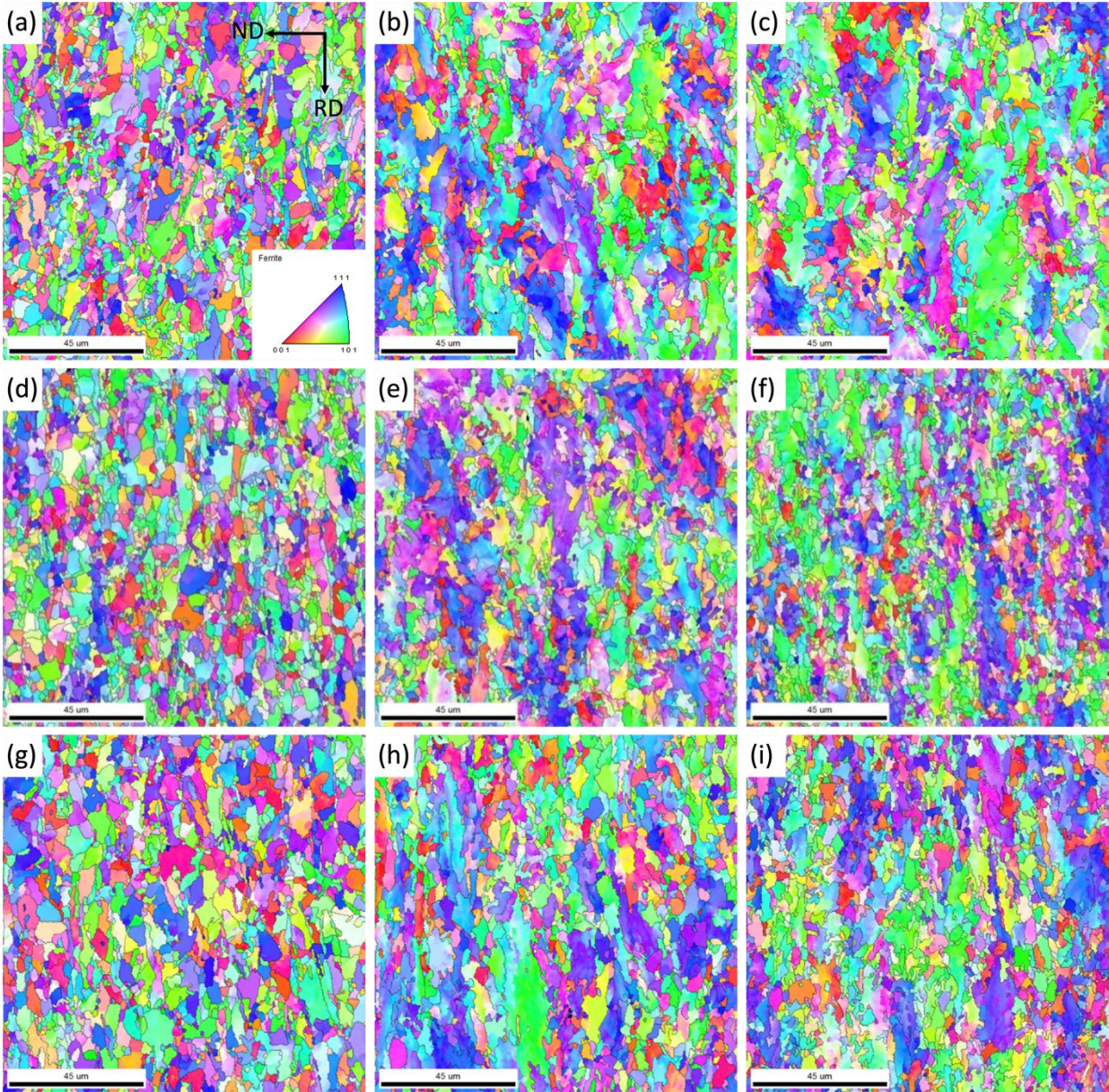
Figure 5. EBSD inverse pole figures (IPF) at steel conditions of: (a) FRT:870°C/ CT:610°C, (b) 870°C/530°C, (c) 870°C/450°C, (d) 810°C/610°C, (e) 810°C/530°C, (f) 810°C/450°C, (g) 750°C/610°C, (h) 750°C/530°C and (i) 750°C/450°C.

Figure 6. EBSD kernel average misorientation (KAM) maps at steel conditions of: (a) FRT:870°C/ CT:610°C, (b) 870°C/530°C, (c) 870°C/450°C, (d) 810°C/610°C, (e) 810°C/530°C, (f) 810°C/450°C, (g) 750°C/610°C, (h) 750°C/530°C and (i) 750°C/450°C.
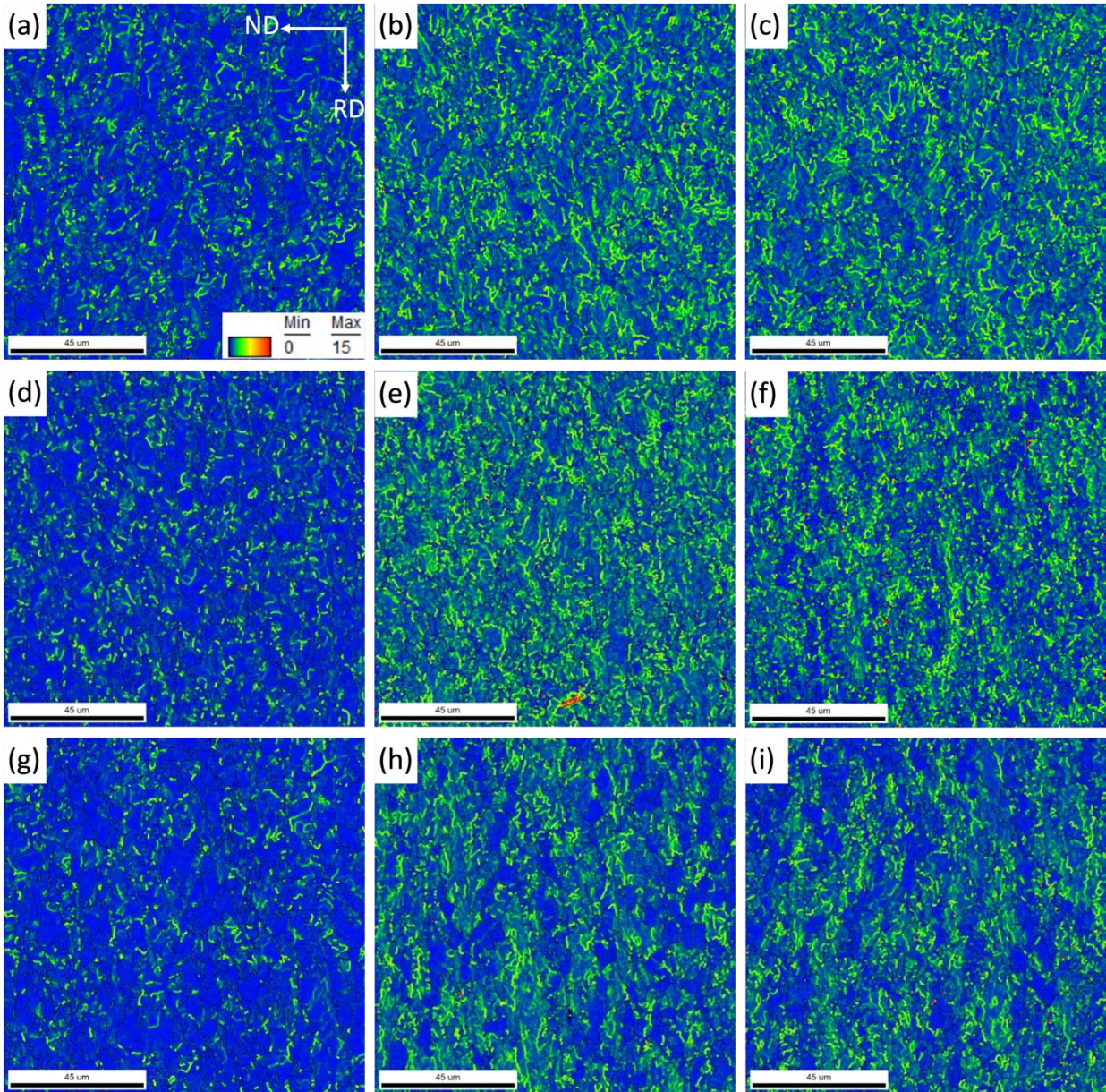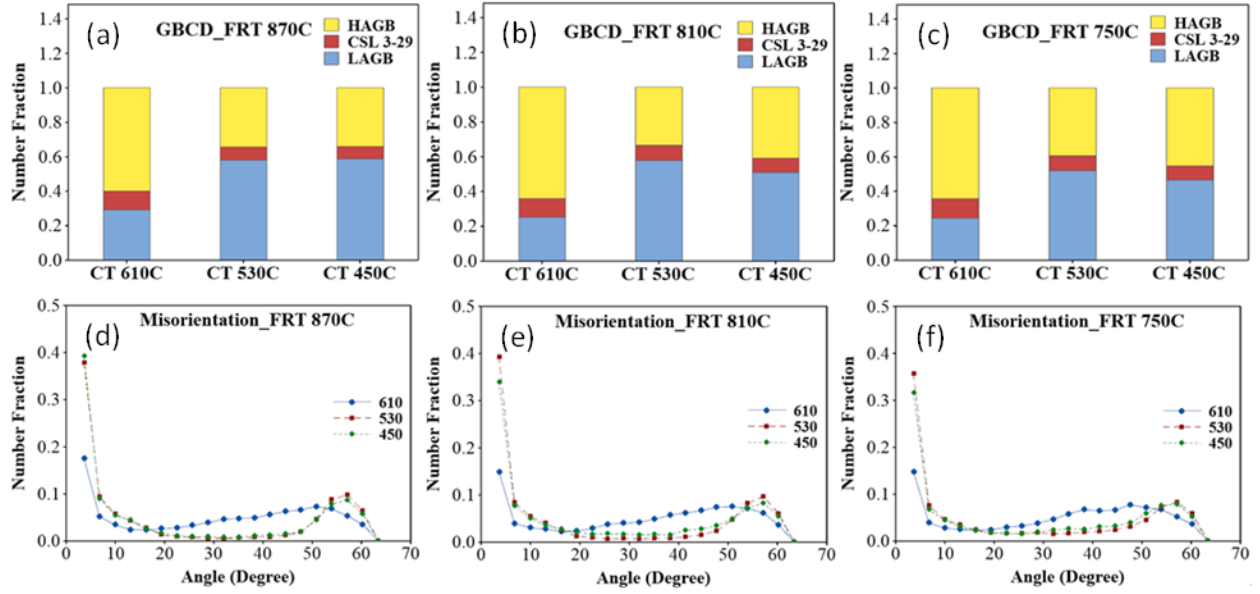
Figure 7. The grain boundary character distributions (GBCD) of the steel conditions with the FRT of (a) 870°C, (b) 810°C and (c) 750°C. The grain boundary misorientation distribution curves of the steel conditions with the FRT of (d) 870°C, (e) 810°C and (f) 750°C.

3.1.2 Precipitation Behavior

For a better observation of the M/A islands and various carbides, an electrolytic etching method was applied [17,18]. The etching was conducted in an alkaline sodium picrate solution at 6 V for 2 to 4 minutes. The ferrite matrix remained unetched, while the fine islands of bainite or carbides, were preferentially etched first and darkened quickly. Once the specimens were etched properly, the M/A constituents appeared as white. As shown in Figure 8 (a), for specimens with a FRT of 870°C and a CT of 610°C, the micrograph indicates neither much bainite, carbides nor M/A constituents in the matrix; only prior austenite grain boundaries appear. However, considering the steel conditions with lower coiling temperatures, a large amount of bainite or carbides was observed, as well as the M/A islands. The differences in microstructures between two lower coiling temperatures are that at the CT of 530°C, the bainite or carbides are distributed relatively uniformly and the M/A islands are fine; while at the CT of 450°C, the carbides become coarser and segregated into bands which are parallel to the rolling direction, also the M/A islands become more frequent and relatively coarser. The volume percentages and the maximum average sizes of M/A for different steel conditions are summarized in Table 2. The maximum average size of M/A particles is defined as the average size of the top 10% of the largest M/A islands in the

10

final microstructures. Table 2 also shows that as the coiling temperature decreases, the volume fraction of M/A constituent increases, as well as the enlarged particle size.
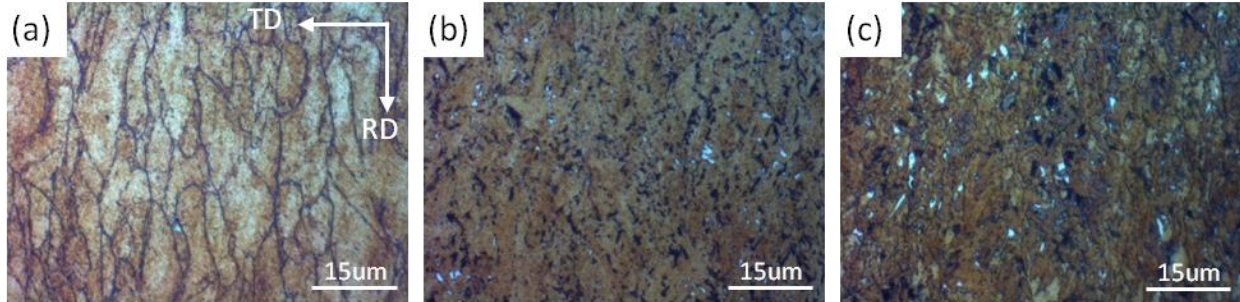

Figure 8. OM micrographs of M/A constituents of the steel conditions: (a) FRT:870°C/ CT:610°C, (b) 870°C/ 530°C and (c) 870°C/ 450°C.

Table 2

The volume fractions (f_V, %) and maximum average sizes (d_{max}, µm) of M/A particles

FRT (ºC)	870	870	870	810	810	810	750	750	750
CT (ºC)	610	530	450	610	530	450	610	530	450
f_v (%)	0	1.1	1.9	0	0.4	1.3	0	0.4	1.8
d_{max} (µm)	N/A	1.2	1.6	N/A	0.9	1.4	N/A	0.9	1.5

During the metallurgical observation, a large amount of particles or inclusions, in addition to the M/A constituents, can be seen on the specimen's surface. From the SEM/EDS results shown in Figure 9, the larger particles are TiN or TiN with an oxide core in the center with a size of several microns and a typical cuboidal shape. The smaller particles are MC or more likely M_2C carbides of approximate composition (Ti, Mo, V)C with a size of a few hundreds of nanometers and a spherical shape. To better observe these particles, dark field optical microscopy was employed and the result from steels with different finishing rolling temperatures but coiled at the same temperature of 610ºC is shown in Figure 10. It can be seen that the all the carbides were located in lines along the rolling direction and the volume fraction of the carbides increased as the FRT decreases.
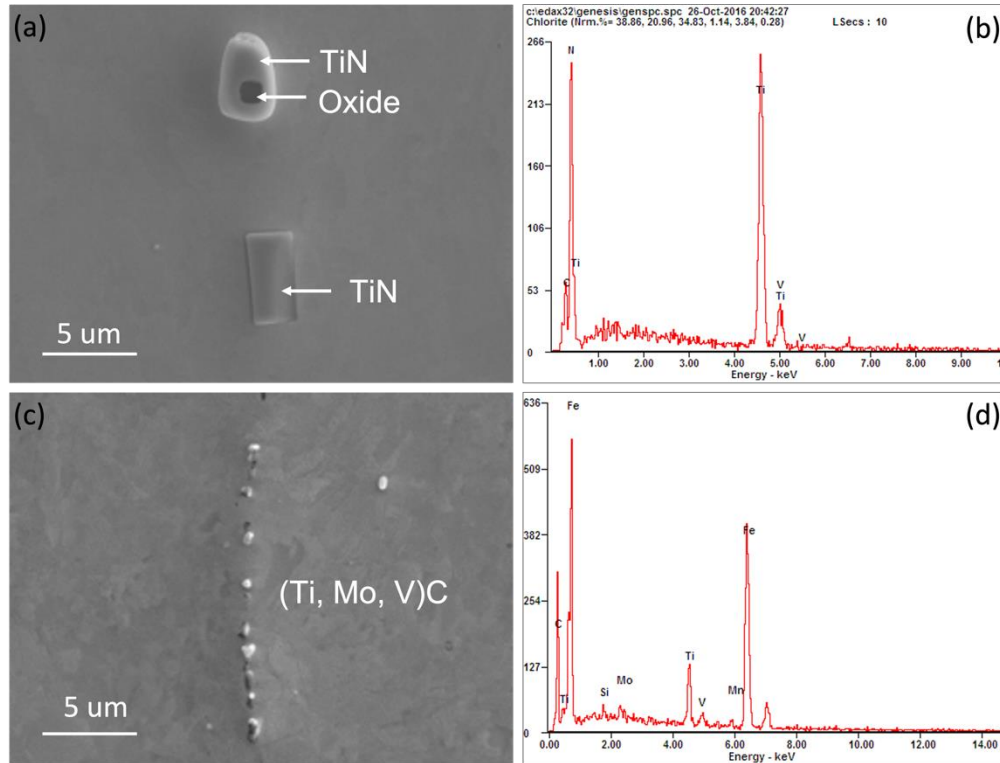
Figure 9. (a) and (b) The SEM micrographs and EDS spectrum of TiN inclusions, (c) and (d) the SEM micrographs and EDS spectrum of (Ti, Mo, V)C inclusions.
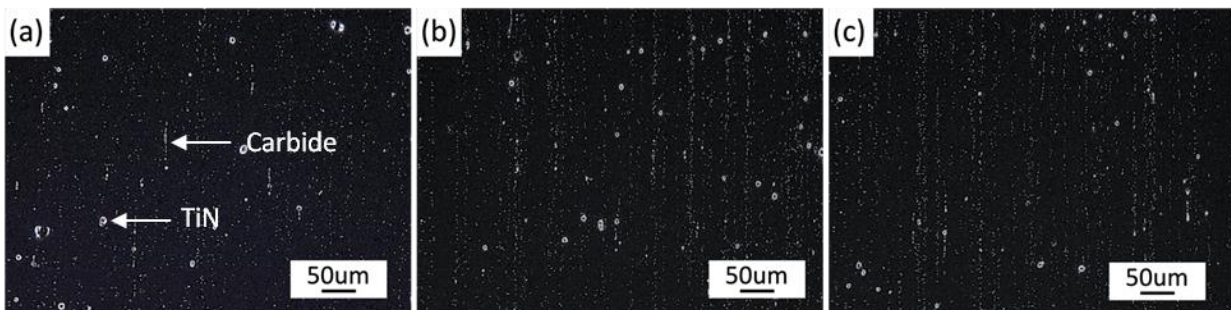

Figure 10. Dark field OM micrographs of the steel conditions: (a) FRT: 870°C/ CT: 610°C, (b) 810°C/ 610°C and (c) 750°C/ 610°C.

The observations shown in Figure 10 led to a further study of precipitation in these conditions using JMatPro predictions. Figures 10 and 11 together revealed three kinds of precipitates TiN, M_2C and MC, where M was found to be approximately M(Ti, Mo, V) using qualitative EDS. The TiN size was about 2-4 µm, the M_2C was in the size range of about 45-900

nm, and the MC was about 10-20 nm. The result of the JMatPro prediction concerning the M_2C and MC precipitation for the three CTs is presented in Figure 11.
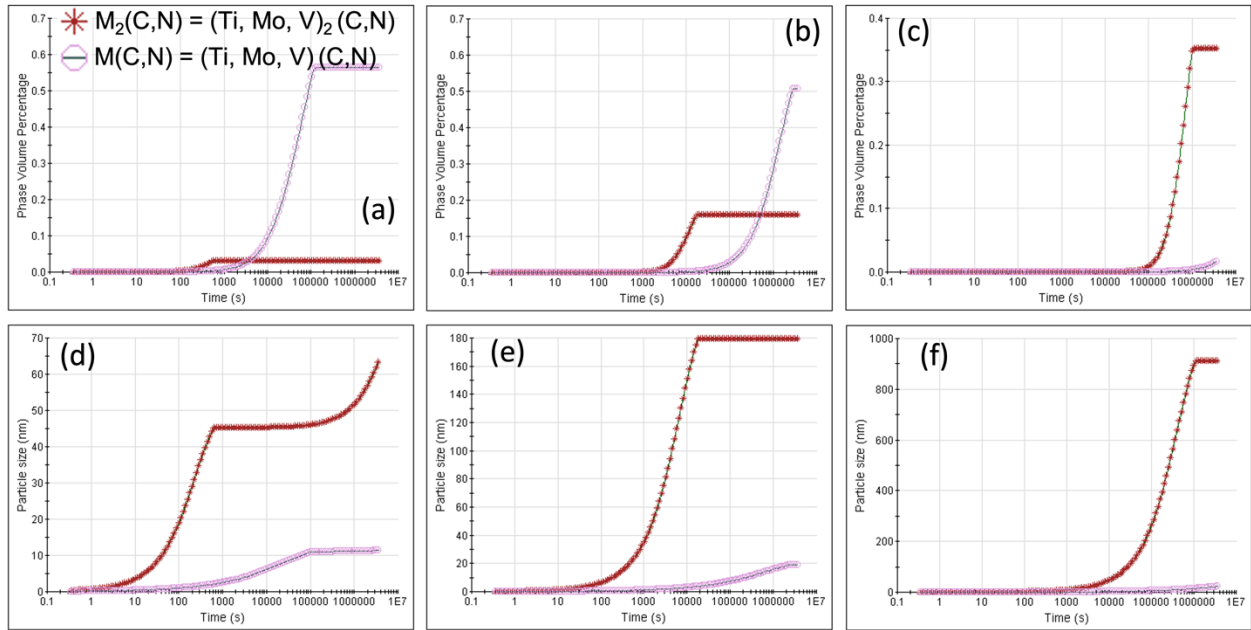

Figure 11. The JMatPro evaluations for the volume fractions and particle sizes of carbonitrides at different CTs of (a) and (d) 610°C, (b) and (e) 530°C, (c) and (f) 450°C.

Note: $M_2(C,N) = (Ti, Mo, V)_2(C,N)$ and $M(C,N) = (Ti, Mo, V)(C,N)$
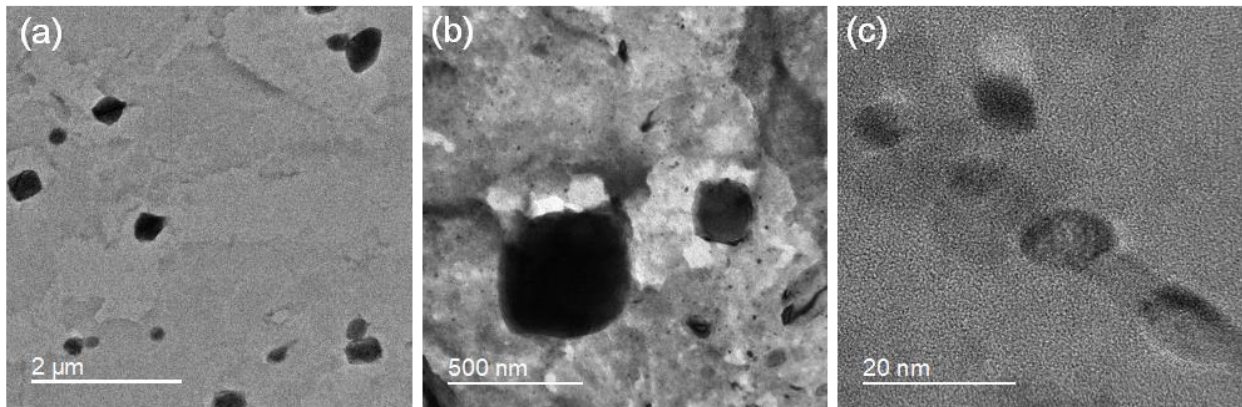

Figure 12. The TEM micrographs of carbon replica for the steel condition FRT: 870°C/ CT: 610°C at different magnifications.

To verify the JMatPro results for precipitation at CT 610°C, TEM of extraction replicas was performed. As predicted in Figure 11, results shown in Figure 12 exhibit two groups of

precipitates, one with a large quantity of large M_2C particles of size from 200 to 500nm (Figure 12 (b), and the other with very small MC particles of size near 10 nm (Figure 12 (c)).

3.2. Mechanical Properties

3.2.1. Tensile properties of the hot band steels

After the microstructural characterization of the hot bands, tensile and hole expansion test were conducted to evaluate the mechanical properties of steel conditions produced from different processing conditions. Figure 13 shows the engineering stress-strain curves for all steel conditions.
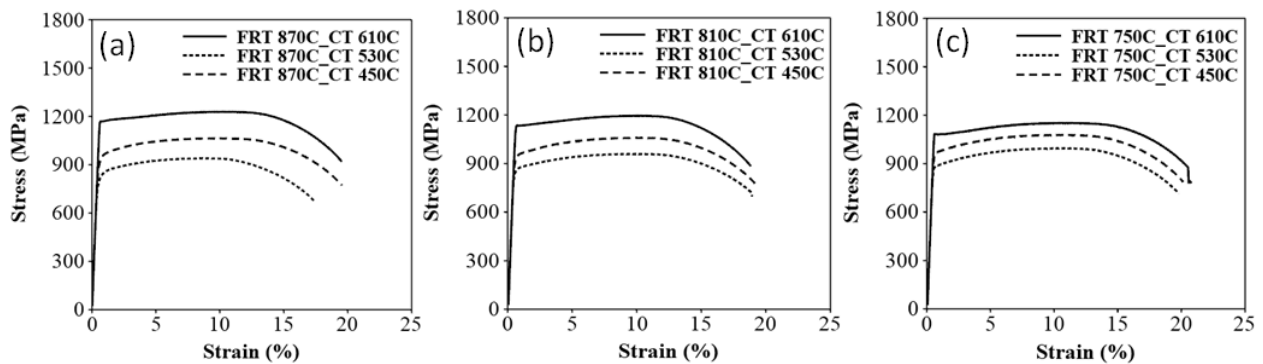

Figure 13. The engineering stress-strain curves of the steel conditions with the FRTs of (a) 870°C, (b) 810°C and (c) 750°C

From Figure 13, the UTS of steel conditions with a CT of 610°C is the highest, with a number around 1200 MPa; and the steel condition with a CT of 450°C has an average value about 1100 MPa; the steel conditions with a CT of 530°C have the lowest UTS value below 1000 MPa. It is obvious that the coiling temperature has an important influence, while the finish rolling temperature was not a major factor in controlling the tensile properties. Meanwhile, the TE of the steels remained relatively constant, ranging from 17 % to 20 %. It seems that the higher strength of the steels did not sacrifice the ductility.

3.2.2 Sheared edge ductility/hole expansion data of the hot band steels

From Table 3, it can be noticed that the hole expansion data show similar values for the steel conditions with the same coiling temperature. During the test, none of the steel conditions with a CT of 610°C survived the hole punching step and the pre-punched hole did not expand at

all in the this test; the hole expansion test (HET) failed with the occurrence of a severe crack on the surface of rolling plane (RD × TD), as shown in Figure 14 (a).

Table 3

The hole expansion ratio (HER, %) of all steel conditions

FRT (℃)	870	870	870	810	810	810	750	750	750
CT (℃)	610	530	450	610	530	450	610	530	450
HER (%)	0	30	5	0	32	7	0	14	5

In terms of the steel conditions with lower coiling temperatures, the HET was not completed until the crack penetrated through the punched and expanded hole surface, as required by the test standard. From Table 3 and Figure 14 (b) and (c), it can be concluded that the hole expansion performances of the steel conditions with the CT of 530°C were better than those of the hot band steels coiled at 450°C.
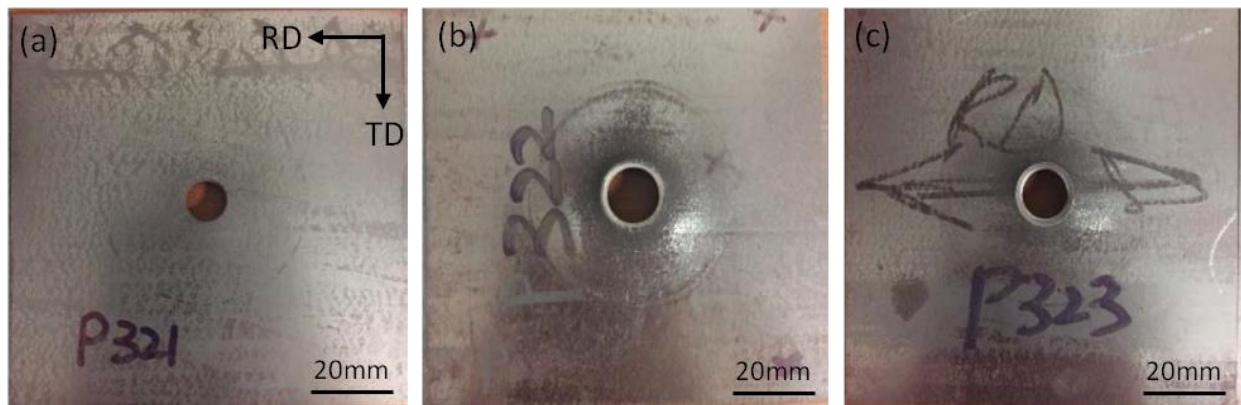
Figure 14. The optical images of the hole expansion specimens: (a) FRT:810°C/ CT:610°C, (b) 810°C/ 530°C; and (c) 810°C/ 450°C.

4. Discussion

4.1 Matrix transformation behavior

As illustrated in Figures 2-4, the microstructures of the hot band were strongly influenced by the CT , the matrix followed a well-recognized pattern with a falling CT, as described by the various classification systems [19–24]. In this study, there were mixtures of ferrite types at each

coiling temperature, but the microstructural evolution trend was clear. For example, concerning the steel conditions with a FRT of 810°C, in Figures 2 (d) and 3 (a), PF, QF and AF were found after coiling at 610°C. In Figures 2 (e) and 3 (b), representing coiling at 530°C, QF, AF, GB and UB and M/A, were observed. After coiling at 450°C, Figures 2 (f) and 3 (c), GB, QF, UB and M/A were found.

The IPF presented in Figure 5 indicated that the ferrite grains formed at CT 610°C were fairly uniform in size with a random distribution of grain orientations. At 530°C, Figures 5 (b), 5 (e) and 5 (h), there appeared both fine PF plus large, elongated QF grains with grain direction normals at or near {101} or {222}. In Figure 5 (f) coiled at 450°C, there were again large grains of ferrite with grain normal orientations at or near {101} or {222}.

The KAM technique is a good way of estimating the local dislocation density of ferrite [25,26]. In Figure 6 (a), the presence of mainly PF is represented in blue signifying a low dislocation/sub-grain boundary density; with some QF in green with higher density; and a little AF in yellow, with even higher dislocation/sub-grain boundary density. With falling CT, it is clear that the amount of PF, QF and AF change with PF declining and QF and AF increasing.

The literature has shown that PF, QF and AF are bounded by high angle grain boundaries [26–29], while GB and UB are not, and their internal dislocation/sub-grain boundary densities are normally taken to be given by the peak height at a few degrees on the grain boundary misorientation distribution plots. Figures 7 (d) to 7 (f) clearly show the change in misorientation along with the CT. The large amount of HAGB found at CT 610°C can be caused by the boundaries between PF, QF or AF because of the high volume fraction and small grain size of the ferrite phase. Moreover, as the microstructures along with the dislocation/sub-grain boundary density develop as the CT falls to lower range, the LAGB increases.

4.2 Precipitation Behavior

As was shown in Figure 8 and Table 2, the M/A constituents, was observed mostly prevalent at the lower CTs. In addition, there were small islands of bainite and individual carbides becoming larger and more segregated in the CT 450°C than 530°C, which could be deleterious to fracture resistance.

In addition to the M/A and bainite constituents, Figures 9-12 revealed particles of TiN, MC and M_2C, where M(Ti,Mo,V) and MC includes TiC, VC and M(Ti,Mo,V)C. The existence of

particles of MC and M_2C was also predicted by JMatPro and is presented in Figure 11. It shows a volume percent of 0.04% with size near 50 nm of M_2C, and a volume percent of 0.57%, with size near 10 nm of MC particles. The small size of MC predicted by JMatpro at the CT of 610°C, led to the TEM results shown in Figure 12, where the MC particles were observed to exhibit a size of 10-20 nm (Figure 12 (c)). These particles would certainly be capable of intense precipitation hardening in the steel with a CT of 610°C; with a precipitation increment in YS of approximately 190 MPa, according to Gladman [30].

4.2.1 Theoretical evaluation of TiN, TiC and VC from solubility products

(i) TiN

Based on the chemical composition of the steel, the hyper-stoichiometric ratio of high levels of Ti and N could cause TiN to form at very high temperatures. Figure 15 shows the phase diagram of the Fe–C system calculated from JMatPro.
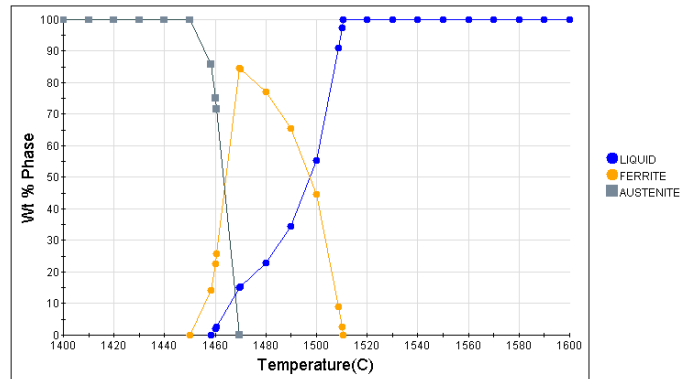

Figure 15. Phase diagram of the Fe – C system calculated from JMatPro.

For TiN nucleate in the liquid, interdendritic pools, the particle is normally very large, several microns in size, and are considered to be inclusions with little strengthening or pinning effect [31,32]. However, when the TiN can nucleate in the solid, they are much smaller in size and can be effective as Zener pinning points for grain size control. The solubility product for TiN in the liquid and austenite can be calculated using Equation 1 and 2 [30,33,34].

$$\log k_s = \log \left([Ti][N] \right)_l = 5.90 - 16586/T \qquad (1)$$

$$\log k_s = \log \left([Ti][N] \right)_\gamma = 4.35 - 14890/T \qquad (2)$$

17

where k_s is the solubility product, [Ti] and [N] are the Ti and N contents dissolved in the liquid in wt.% and T is the absolute temperature in K, the phase transformation temperatures are dictated from Figure 16, and the calculated result of volume fraction of TiN (f_v) are presented in Table 4, and the detailed calculation process can be seen in [35]. From Table 4, it is obvious that N would be nearly completely consumed to form the TiN precipitated in austenite at the reheating temperature of 1200°C, and the rest of the Ti, which would remain in solution after reheating, would be 0.1425 wt.%. Since the volume fraction of TiN precipitated does not change much from reheating to finish rolling, little strain-induced precipitation of TiN would be expected during rolling.

Table 4

Calculated solubility product (k_s), remaining Ti and N contents in solution and volume fraction (f_v) of TiN precipitated in liquid and austenite varying with temperature.

T (°C)	Matrix	$k_s \times 10^4$	$[Ti] \times 10^3$	$[N] \times 10^3$	$f_v \times 10^4$
In liquid, $[Ti]_{initial} \times 10^3 = 163.00$ and $[N]_{initial} \times 10^3 = 6.00$					
1510	Liquid	3.96	151.42	2.61	2.18
1458	Liquid	2.08	147.31	1.41	2.96
In austenite, $[Ti]_{initial} \times 10^3 = 147.31$ and $[N]_{initial} \times 10^3 = 1.41$					
1450	Austenite	0.51	143.70	0.36	0.68
1200	Austenite	0.02	142.53	0.01	0.90
871	Austenite	2.16×10^{-5}	142.49	1.52×10^{-5}	0.91

(ii) TiC

Based on the chemical composition and solubility product of Ti and C, TiC would not be expected to form in the liquid. In terms of TiC forming in austenite, the solubility product of TiC in austenite is expressed by Equation 3 [36].

$$\log k_s = \log \left([Ti][C] \right)_\gamma = 2.75 - 7000/T \tag{3}$$

If we take [Ti] and [C] as 0.14731 wt.% and 0.140 wt.%, respectively, the dissolution temperature of TiC in austenite will be 1578K (1305°C), lower than the fully austenitic formation temperature at 1450°C. This predicts that TiC precipitation in austenite would occur at or slightly below 1305 °C. Therefore, the calculated volume fraction of TiC inclusions in austenite is shown in Table 5. It

predicts a relatively large amount of strain-induced precipitate of TiC in austenite during hot rolling, which explains the pancaked grain shapes observed in the OM of Figure 8 (a).

Table 5

Calculated solubility products (k_s), remaining Ti and C contents in solution and volume fraction (f_v) of TiC precipitates in austenite varying with temperatures.

T (°C)	Matrix	$k_s \times 10^4$	$[Ti] \times 10^3$	$[C] \times 10^3$	$f_v \times 10^4$
In austenite, $Ti_{initial} \times 10^3 = 147.31$ and $C_{initial} \times 10^3 = 140.00$					
1305	Austenite	206.07	147.21	139.98	0.02
1200	Austenite	99.49	80.69	123.30	13.38
871	Austenite	4.28	4.11	104.11	28.75

(iii) VC

If VC inclusions or particles formed in ferrite, then the solubility product of VC in ferrite can be calculated using Equation 4 [37].

$$\log k_s = \log([V][C])_\alpha = 8.05 - 12230/T \tag{4}$$

If it is assumed that all the vanadium and the remaining carbon in solution after the TiC precipitation were dissolved in ferrite, then [V] is 0.294 wt.% and the remaining [C] in ferrite is 0.10411 wt.%. Therefore, the dissolution temperature of VC in ferrite is 1250K (977°C), which is above the A_{r3}. The volume fraction of VC in ferrite at various temperatures is listed in Table 6.

Table 6

Calculated solubility product (k_s), remaining V and C contents and volume fraction (f_v) of VC precipitates in ferrite varying with temperature.

T (°C)	Matrix	$k_s \times 10^4$	$[V] \times 10^3$	$[C] \times 10^3$	$f_v \times 10^4$
In ferrite, $V_{initial} \times 10^3 = 294.0$ and $C_{inital} \times 10^3 = 104.11$					
871	Ferrite	22.88	49.31	46.40	26.20
610	Ferrite	0.02	0.05	34.78	31.48

After theoretical calculation, the solute contents remaining in solution in the ferrite after all of the precipitation would be approximately 0 for nitrogen, 0.00411 wt.% for titanium, 0.03478 wt.% for carbon and 0.00005 wt. % for vanadium.

4.2.2 Electron microscopy observation

These simulated results show that there is a large amount of precipitates with a small particle size formed at the highest coiling temperature, and the solubility product calculation also reveals that the Ti and V could precipitate as fine, dispersed carbide particles during the hot rolling of the austenite or in the ferrite during coiling.

Evidence of this was exhibited in Figure 16. For MC to form in ferrite, it must have both the thermodynamic driving force to form the particles and sufficiently high diffusivity to permit the atom movements necessary for the precipitation reaction. This latter requirement might be one reason why less or no fine precipitate was found at the lower coiling temperatures. Figure 16 (a) shows fine precipitates with a similar size to the M(Ti, Mo, V)C particles shown in Figure 12 (c). Comparing Figures 16 (a) to (c), it is obvious that the condition with a coiling temperature of 610°C shows a large volume fraction of fine precipitates, and conditions with lower coiling temperatures, there are not many precipitates observed on the carbon replicas.
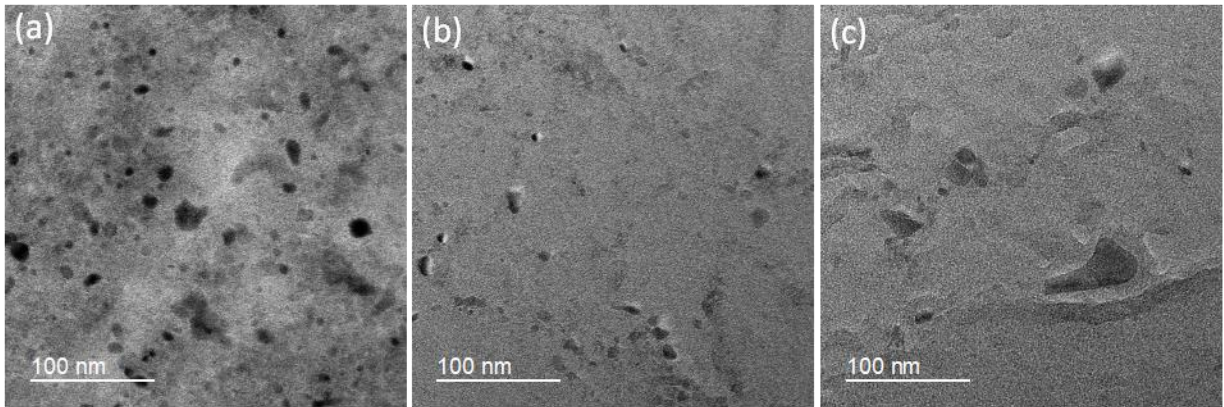

Figure 16. The TEM carbon replica of the precipitates in the steel conditions: (a) FRT: 870°C/ CT: 610°C, (b) 870°C/ 530°C and (c) 870°C/ 459°C.

4.3 Mechanical Properties
4.3.1 Hot band properties

Typically, the strength of the hot band will increase as the coiling temperature decreases due to the formation of stronger low temperature transformation products with falling coiling temperature. Normally, the steels with a polygonal ferrite microstructure at CT of 610°C should have the lowest strength, and the steels with a CT of 450°C which consist of bainite, quasi-polygonal ferrite and M/A constituents should have the highest strength. But in this study, the strength and CT are not inversely related.

The explanation for this unusual observation lies in the nature of the various microstructures formed at different CTs. As noted above, due to the higher driving force and adequate diffusivity, CTs at or above 600°C normally exhibit polygonal ferrite microstructures [38] that often form strengthening precipitates MX, where M represents the cation Nb, V or Ti, and X represents the anion C or N. In addition, the stress-strain curves from Figure 13 show yield points for the conditions with a CT of 610°C, while the conditions with lower CTs exhibit continuous yielding behaviors. As is well-known, the appearance of a yield point occurs when the ratio of solute carbon to glissile dislocations is high, which leads to an upper yield point [39–41]. These yield points can be easily removed either by carbon stabilization or by temper rolling. The stabilization removes the carbon from solution and the temper rolling increases the dislocation density. A similar effect occurs with the formation of low temperature ferrite, which forms with a high dislocation density [42,43]. Yield points are not observed in carbon steels containing bainite or martensite, regardless of carbon content. Therefore, the presence of the yield point means that an additional strengthening mechanism must be considered; the interstitial solute hardening of the ferrite caused by carbon that has not been tied up as MC during the coiling treatment at 610 °C.

Figure 17 shows the plot of the tensile and yield strength data of all the steel conditions. It shows the effect of the FRT on the strength. For the steels with low coiling temperatures, the strength increases with the decrease of the FRT which can be explained by the more deformed matrix and higher dislocation density brought by the lower FRT. However, for the steels with a CT of 610°C, the trend is in an opposite way, such that the strength decreases with the decrease of the finish rolling temperature. This could be explained by Figure 10 where it shows the volume fraction of those strain-induced coarser precipitates increases as the FRT decreases which would result in less potential to form fine precipitates during coiling at 610°C. Furthermore, the absence of MA microconstituent means that only minor work hardening of the ferrite can be expected in

the tensile test. This causes only a small increase between the YS and the UTS, as shown in Figure 17.

From the discussion so far, it is known that the high UTS strength of the steels with the high CT of 610°C is due to the combination of a high YS caused by fine ferrite grain size and the copious, fine precipitates formed during coil cooling, and also remained carbon in solution in the ferrite, but the low additional strengthening is due to the weak work hardening.
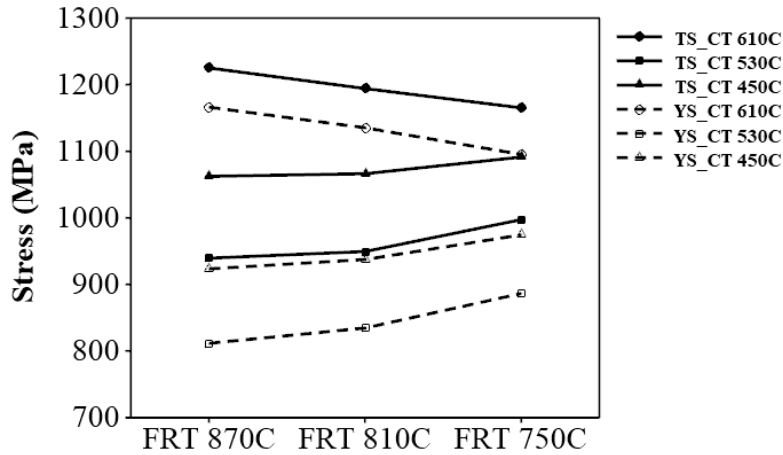

Figure 17. The Comparisons of the UTS and YS values of the steel conditions varying with processing parameters.

4.3.2 Strengthening mechanism contribution

To help explain the origin of the strengths observed, we will use Expanded Hall-Petch relation expressed by Equation 5,

$$\sigma_Y = \sigma_o + \Delta\sigma_S + \Delta\sigma_G + \Delta\sigma_D + \Delta\sigma_P \tag{5}$$

where, σ_Y is the measured yield strength, σ_o is the lattice friction or Peierls-Nabarro stress and $\Delta\sigma_S$, $\Delta\sigma_G$, $\Delta\sigma_D$ and $\Delta\sigma_P$ are the contributions from solid solution, ferrite grain refinement, dislocation density and fine precipitates in ferrite matrix, respectively.

The contribution from the lattice friction is about 48 MPa [7]. And from the chemical composition and solubility product estimation, the calculated contribution from solid solution hardening is about 243 MPa [44,45]. Since the Hall-Petch relationship [46] describes the strengthening of ferrite by HAGBs, from the EBSD results, the steels with a CT of 530°C always exhibit the coarsest microstructures, and steels with a CT of 450°C show the finest microstructures.

Take the steels with a FRT of 750°C as examples, the steels coiled at 530°C make 305 MPa strengthening contribution to the total strength, while steels with CTs of 610 °C and 450°C contribute 320MPa and 330 MPa, respectively.

From previous results, including the observation from the dark field OM and TEM replicas, the simulation from JMatPro, also the stress-strain curve from tensile test, it is apparent that higher strength in the condition with the CT of 610°C is due to the formation of fine precipitates during in-coiling cooling, and the finer particle MC is the main contributor. From the data extracted from Figure 11, the contribution to strength from the precipitates which had been hypothetically quenched from 870°C and held at different temperatures is calculated by Equation 6 [44] and the data is shown in Table 7.

$$\Delta\sigma_P = 8.995 \times 10^3 \frac{f^{\frac{1}{2}}}{d} \ln(2.417d) \tag{6}$$

where f is the volume fraction and d is the particle size in nm.

Table 7

Strengthening contribution ($\Delta\sigma_P$, MPa) from different types of carbides precipitates

CT (°C)	MC	M$_2$C	Total
610	201	19	220
530	64	12	76
450	6	2	8

From Table 7, it can be seen that at the coiling temperature of 610°C, the total contribution from precipitation is 220 MPa, of which 201 MPa is coming from finer MC carbides. Verifying this calculation using the Gladman approach [30] resulted in a precipitation strengthening increment of 190 MPa for the MC particles with a CT of 610°C. It is clear from Table 7 that the particle strengthening coming from the conditions of lower coiling temperature is much smaller; 76 MPa from 530°C and 8 MPa from 450°C. At each holding or coiling temperature, the MC carbides are responsible for the preponderance of the particle strengthening. Figure 17 also shows the volume fraction of precipitates at different CT, if we take the 10 nm as the size of the precipitates in Figure 17 (a), the volume fraction in Figure 11 (a) and apply Equation 6, the $\Delta\sigma_P$ can be calculated to be about 200 MPa.

The steel condition with lower coiling temperatures did not exhibit much strengthening from the fine precipitates, so the strength is mainly associated with other aspects of the microstructures. As discussed before, quasi-polygonal ferrite and bainite start to form in the steels with lower coiling temperatures, and from Figure 6, those conditions with phases which are inherited with high dislocation densities that could improve the strength.

Since misorientation within 2° is related to the dislocation densities [47], so here KAM with maximum misorientation degree of 2° was applied to evaluate the dislocation densities in steels with different CTs and the results are shown in Figure 18. From Figures 18 (a) to (c), it shows as the CT decreases, the areas of regions with higher misorientation increases, so does the dislocation density. To calculate the dislocation density and strength contribution, Equation 7 and 8 are applied, and the results are shown in Table 8 [47–50].

$$\rho = \frac{2HRKAM}{bu} \tag{7}$$

$$\Delta\sigma_D = M\alpha Gb\sqrt{\rho} \tag{8}$$

where ρ is the dislocation density, HRKAM is high resolution KAM converted from conventional KAM in rad, b is the burgers (b= 0.248 nm) vector and μ is the step size (u = 100 nm), M is the Taylor factor (M=1.84), α is a constant dependent on structure (α=0.24), G is the shear modulus (G=83 GPa)

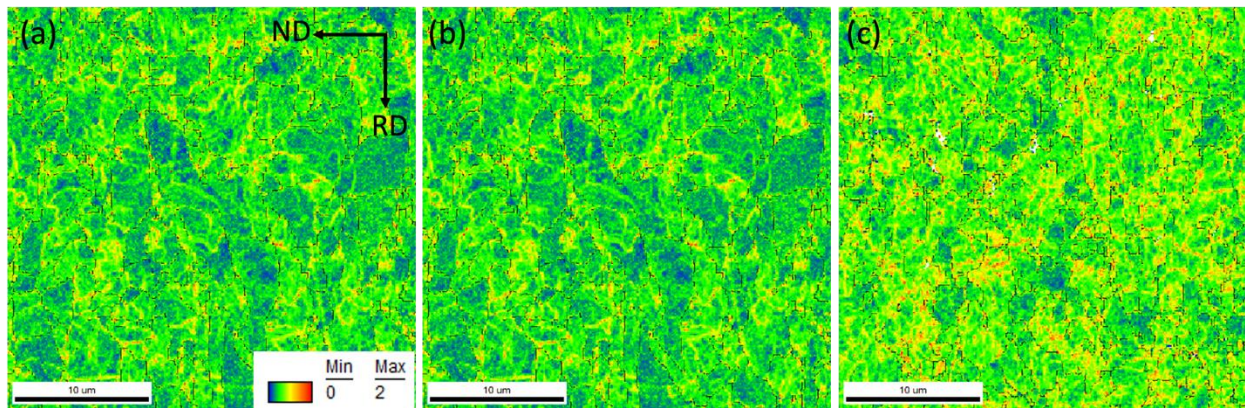**Figure 18.** The KAM maps of the steel conditions: (a) FRT:810°C/ CT:610°C, (b) 810°C/ 530°C and (c) 810°C/ 450°C.

Table 8

Dislocation density (ρ, m^{-2}) from HRKAM

FRT (ºC)	810	810	810
CT (ºC)	610	530	450
ρ(m^{-2})	6.3E+14	8.0E+14	8.6E+14
$\Delta\sigma_D$(MPa)	228	257	267

It can be seen from this table, the contribution to the yield strength from dislocation density increases as the CT decreases. However, although Figure 19 shows a clear increase in the KAM for the conditions with lower CTs, the $\Delta\sigma_D$ does not show much difference as expected, this is probably due to the quality of the EBSD scanning result.

Therefore, from previous discussion, it can be concluded that the highest strength from conditions with a CT of 610ºC is due to the fine ferrite grain size plus the formation of a large amount of fine precipitates during coiling. For steels with a CT of 530ºC, because of the coarser grain size, intermediate level of dislocation strengthening, much less amount of fine precipitates, neither of the strengthening mechanisms mentioned above predominate at that CT, which result in the lowest strength. Even though there was an fairly amount of MA micro-constituents and M_2C formed at this CT, which can interact with dislocations and resulted in substantial work hardening, this increase would not compensate for the low YS observed in this steel condition. Coiling at 450ºC resulted in a fine microstructure based on the small separation of HAGBs. This, together with the high dislocation density and high solute carbon content, would be expected to result in an intermediate YS level, but also a high level of work hardening caused by the large M_2C particles (Figure 11) and the high amount of large MA particles, Table 2 and Figure 8.

4.4 Sheared Edge Ductility/ Hole Expansion Properties

As illustrated in Table 3, the steel conditions with the same CT have similar HER results. And the data show an inverse correlation with the tensile properties, which conforms to the earlier published investigations [6,51].

In this study, it is surprising that the overall HER values were lower than expected, even though the final microstructures consisted mainly of PF and QF, especially for steels with a CT of

610°C, instead of penetrating through the thickness, the cracks occurred on the rolling plane, Figure 19 (a).

The literature in HER studies shows that the through-thickness cracks were often associated with (i) the decohesion of the ferrite/ hard phase constituents interfaces, (ii) martensite cracking, (iii) ferrite/ferrite boundaries near the punched hole surfaces and (iv) MnS inclusions or or other second phase precipitate particles (i.e., TiO or TiN) [52–55]. These mechanisms can also be applied in this situation. During the hole expanding test, the upper sheet surface was under tension due to the upward bending brought by the contact with the conical punch, and the TiN particles can act as a stress concentrator, promote the crack formation by either being cracked themselves or decohering from the ferrite matrix. The cracks formed either after hole punching or during the expanding process would then be linked through propagation until final failure, Figure 19 (c) and (d).
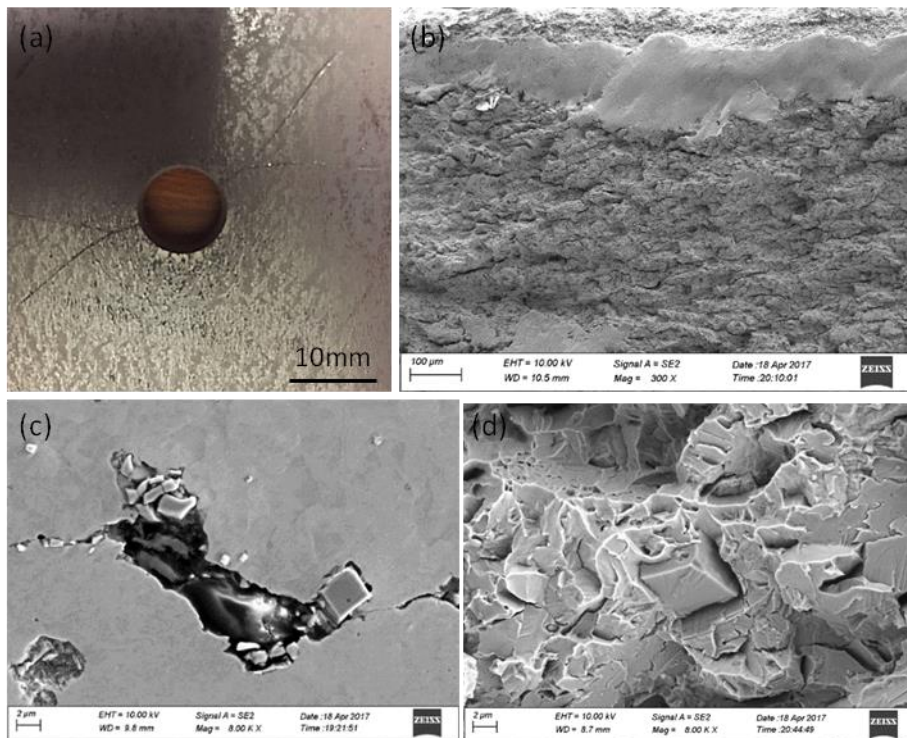

Figure 19. Surface crack and fracture surface of a hole expansion specimen (FRT:810°C/ CT:610°C) with 0% HER: (a) the cracks appearing on the rolling surface, (b) the fracture surface of the cracks observed in the rolling plane, and coarse TiN precipitates observed in the (c) rolling plane and (d) fracture surface.

A higher strength matrix will have less accommodation ability to relieve the concentrated stress brought by the TiN particles. Figure 19 (b) shows a smooth region on the fracture surface located underneath the free surface which indicates a brittle fracture of this sudden failure because of the ultra high strength of the steels with a CT of 610°C. Therefore, a high dislocation densities or volume percentages of sub-grain structures could also have negative influences on hole expansion behaviors which would explain the difference in HER between the steels with CT 530°C and CT 450°C.

5. Conclusions

Ultra-high strength hot band steels were produced and investigated in this study. The analysis was based on the microstructure characterization and mechanical tests. Several conclusions have been drawn as follows:

1. The finish rolling temperature does not have obvious effects on the microstructure. However, the microstructure in the matrix was observed to change from mainly polygonal ferrite to quasi-polygonal ferrite to granular bainite and upper bainite, accompanied by the formation of martensite/austenite constituents as coiling temperature falls.

2. The high strength in the steels with the highest coiling temperature of 610°C is attributed to the 10 nm precipitates including TiC, VC and M(Ti, Mo, V)C precipitates formed during coiling process. The higher strength of the steels with the lowest coiling temperature of 450°C is due to the higher dislocation density coming from acicular ferrite, quasi-polygonal ferrite, and bainitic ferrite grains.

3. The strain-induced precipitates cannot increase the strength of the steel because of the large particle size, and the volume fraction of those precipitates will increase as the finish rolling temperature decreases.

4. Due to the hyper-stoichiometric ratio of Ti and N which cause TiN precipitates nucleate at very high temperature and form a large size, along with other hard phases, like M/A constituents and bainite, the hole expansion ratio is relatively low.

5. Further suggestions to improve the mechanical properties of the steel should be made on the controlling of the appropriate solubility product. Excessively large amounts of precipitates, inclusions, and M/A constituents can be harmful to ductility and formability.

Acknowledgements

References

[1]   B.K. Zuidema, S.G. Denner, B. Engl, J.-O. Sperle, New high strength steels applied to the body structure of ULSAB-AVC, in: 2001 SAE Int. Body Eng. Conf., 2001: pp. 1–10. https://doi.org/10.4271/2001-01-3042.

[2]   J. Galán, L. Samek, P. Verleysen, K. Verbeken, Y. Houbaert, Advanced high strength steels for automotive industry, Rev. Metal. 48 (2012) 118–131. https://doi.org/10.3989/revmetalm.1158.

[3]   R. Kuziak, R. Kawalla, S. Waengler, Advanced high strength steels for automotive industry, Arch. Civ. Mech. Eng. 8 (2008) 103–117. https://doi.org/10.1016/S1644-9665(12)60197-6.

[4]   S. Dinda, R. Diaz, The partnership for a new generation of vehicles (PNGV) and its impact on body engineering, in: IBEC'95-Advanced Technol. Process., 1995.

[5]   A. Jambor, M. Beyer, New car-new materials, Mater. Des. 18 (1997) 203–209.

[6]   O.R. Terrazas, K.O. Findley, C.J. Van Tyne, Influence of martensite morphology on sheared-edge formability of dual-phase steels, ISIJ Int. 57 (2017) 937–944. https://doi.org/10.2355/isijinternational.ISIJINT-2016-602.

[7]   R. Wang, C.I. Garcia, M. Hua, K. Cho, H. Zhang, A.J. Deardo, Microstructure and precipitation behavior of Nb, Ti bomplex microalloyed steel produced by compact strip processing, ISIJ Int. 46 (2006) 1345–1353. https://doi.org/10.2355/isijinternational.46.1345.

[8]   A.J. DeArdo, M.J. Hua, K.G. Cho, C.I. Garcia, On strength of microalloyed steels: an interpretive review, Mater. Sci. Technol. 25 (2009) 1074–1082. https://doi.org/10.1179/174328409X455233.

[9]   B.K. Show, R. Veerababu, R. Balamuralikrishnan, G. Malakondaiah, Effect of vanadium and titanium modification on the microstructure and mechanical properties of a microalloyed HSLA steel, Mater. Sci. Eng. A. 527 (2010) 1595–1604. https://doi.org/10.1016/j.msea.2009.10.049.

[10]   L. Xu, F. Barlat, K. Choi, X. Sun, Hole expansion of dual phase steels, in: WIT Trans. Built Environ., 2012: pp. 75–83.

[11]   G. Em Totten, L. Xie, K. Funatani, Handbook of Mechanical Alloy Design, CRC Press, 2003. https://doi.org/10.1201/9780203913307.

[12]   T. Shimizu, Y. Funakawa, S. Kaneko, High strength steel sheets for automobile suspension and chassis use - High strength hot-rolled steel sheets with excellent press formability and durability for critical safety parts, 2004.

[13]   Nissan to use ultrastrong, high-formability steel in more new vehicles World-first innovation can help lower emissions and improve performance by reducing vehicle weight, M2 Press. (2018) 1–3. http://bi.gale.com.pitt.idm.oclc.org/global/article/GALE%7CA543359344? u=upitt_main.

[14]   R.A. Rijkenberg, A. Blowey, P. Bellina, C. Wooffindin, Advanced High Stretch-Flange Formability Steels for Chassis & Suspension Applications, in: 4th Int. Conf. Steels Cars Truck., Braunschweig, Germany, 2014: pp. 426–433.

[15]   P.A. Soloski, N.J. Thimons, A.A. Marks, J. Hartle, Q. Trest, A. Johnston, W. Perisse, A.J. DeArdo, Sheared-edge ductility / hole-expansion ratio testing of advanced high-strength steels, in: Mater. Sci. Technol. 2015, Columbus, 2015: pp. 917–926.

[16]   ISO/TS 16630:2003 Metallic materials-method of hole expanding test, 2003.

[17]   E. Bonnevie, G. Ferrière, A. Ikhlef, D. Kaplan, J.M. Orain, Morphological aspects of martensite–austenite constituents in intercritical and coarse grain heat affected zones of structural steels, Mater. Sci. Eng. A. 385 (2004) 352–358. https://doi.org/10.1016/j.msea.2004.06.033.

[18]   H. Ikawa, H. Oshige, T. Tanoue, Effects of martensnite-austennite on HAZ toughness of a high strength steel, in: Trans. Japan Weld. Soc., 1980: pp. 87–96.

[19]   G. Krauss, Ferritic Microstructures, in: Steels Process. Struct. Perform., Materials Park, Ohio, 2005: pp. 101–118. https://doi.org/10.1361/spsap2005p101.

[20]   H.I. Aaronson, The proeutectoid ferrite and the proeutectoid cementite reactions, in: V.F. Zackay, H.I. Aaronson (Eds.), Decompos. Austenite by Diffus. Process., Interscience, New York, 1962: pp. 387–548.

[21]   H. Ohtani, S. Okaguchi, Y. Fujishiro, Y. Ohmori, Morphology and properties of low-carbon bainite, Metall. Trans. A. 21 (1990) 877–888. https://doi.org/10.1007/BF02656571.

[22]   B.L. Bramfitt, J.G. Speer, A perspective on the morphology of bainite, Metall. Trans. A. 21 (1990) 817–829. https://doi.org/10.1007/BF02656565.

[23]   T. Araki, I. Kozasu, H. Tankechi, K. Shibata, M. Enomoto, H. Tamehiro, Atlas for bainitic microestructures, Tokyo, Japan, 1992.

[24]   E.A. Wilson, The γ→ α transformation in low carbon irons, ISIJ Int. 34 (1994) 615–630. https://doi.org/10.2355/isijinternational.34.615.

[25]   M. Calcagnotto, D. Ponge, E. Demir, D. Raabe, Orientation gradients and geometrically necessary dislocations in ultrafine grained dual-phase steels studied by 2D and 3D EBSD, Mater. Sci. Eng. A. 527 (2010) 2738–2746. https://doi.org/10.1016/j.msea.2010.01.004.

[26]   C. Fang, C.I. Garcia, S.-H. Choi, A.J. DeArdo, A Study of the batch annealing of cold-rolled HSLA steels containing niobium or titanium, Metall. Mater. Trans. A. 46 (2015) 3635–3645. https://doi.org/10.1007/s11661-015-2949-6.

[27]   N.Y. Zolotorevsky, V.V. Rybin, E.A. Ushanova, Analysis of grain misorientation distribution in polygonal ferrite of low-carbon steel, Mater. Charact. 122 (2016) 70–75. https://doi.org/10.1016/j.matchar.2016.10.022.

[28]   H. Zhao, B.P. Wynne, E.J. Palmiere, Conditions for the occurrence of acicular ferrite transformation in HSLA steels, J. Mater. Sci. 53 (2018) 3785–3804. https://doi.org/10.1007/s10853-017-1781-3.

[29]   Y.M. Kim, H. Lee, N.J. Kim, Transformation behavior and microstructural characteristics of acicular ferrite in linepipe steels, Mater. Sci. Eng. A. 478 (2008) 361–370. https://doi.org/10.1016/j.msea.2007.06.035.

[30]   T. Gladman, The Physical Metallurgy of Microalloyed Steels, 1997.

[31]   T. Siwecki, A. Sandberg, W. Roberts, Processing Characteristics and Properties of Ti–V–N steels, in: Int. Conf. Technol. Appl. HSLA Steels, Am., American Society of Metals, 1983: pp. 619–634.

[32]   S.C. Wang, The effect of titanium and nitrogen contents on the austenite grain coarsening temperature, J. Mater. Sci. 24 (1989) 105–109. https://doi.org/10.1007/BF00660940.

[33]   K. Inoue, I. Ohnuma, H. Ohtani, K. Ishida, T. Nishizawa, Solubility product of TiN in austenite., ISIJ Int. 38 (1998) 991–997. https://doi.org/10.2355/isijinternational.38.991.

[34]   L.F.S. Dumitrescu, M. Hillert, Reassessment of the solubility of TiC and TiN in Fe., ISIJ Int. 39 (1999) 84–90. https://doi.org/10.2355/isijinternational.39.84.

[35]   Ma, Bing (2017) A Study of Processing, Microstructure and Mechanical Properties of Ultra-High Strength Microalloyed Steel Hot Band Coils for Automotive Applications. Doctoral Dissertation, University of Pittsburgh. http://d-scholarship.pitt.edu/32587/.

[36]   K.J. Irvine, F.B. Pickering, T. Gladman, Grain-refined C-Mn steels, J. Iron Steel Institue. 205 (1967) 161–182.

[37]   R. Langeborg, T. Siwecki, S. Zajac, B. Hutchinson, Role of vanadium in microalloyed steels, Scand. J. Metall. 28 (1999) 186–241.

[38]   Gong, Yu, et al. "Influence of processing factors on the sheared-edge formability of vanadium bearing dual-phase steels produced using continuous galvanizing line simulations." Journal of Materials Science 55.13 (2020): 5639-5654. https://doi.org/10.1007/s10853-020-04385-0

[39]   G. E. Dieter, Mechanical Metallurgy, 1986, McGraw-Hill, Boston, pp 197-203.

[40]   W. C. Leslie, The Physical Metallurgy of Steels, 1981, Hemisphere Publishing, pp 134-162.

[41]   A.H. Cottrell, B.A. Bilby, Dislocation theory of yielding and strain ageing of iron, Proc. Phys. Soc. Sect. A. 62 (1949) 49–62. https://doi.org/10.1088/0370-1298/62/1/308.

[42]   R.G. Davies, Early stages of yielding and strain aging of a vanadium-containing dual-phase steel, Metall. Trans. A. 10 (1979) 1549–1555. https://doi.org/10.1007/BF02812021.

[43] N.J. Kim, A.J. Yang, G. Thomas, Effect of finish rolling temperature on the structure and properties of directly quenched Nb containing low carbon steel, Metall. Trans. A. 16 (1985) 471–474. https://doi.org/10.1007/BF02814349.

[44] Q. Yong, Secondary phases in steels, Metall. Ind. Press. Beijing. (2006) 83.

[45] X. Zhang, C. Loannidou, G.H. ten Brink, A. Navarro-López, J. Wormann, J. Campaniello, R.M. Dalgliesh, A.A. van Well, S.E. Offerman, W. Kranendonk, B.J. Kooi, Microstructure, precipitate and property evolution in cold-rolled Ti V high strength low alloy steel, Mater. Des. 186 (2020) 108720. https://doi.org/10.1016/j.matdes.2020.108720.

[46] E.O. Hall, The deformation and ageing of mild steel: III discussion of results, Proc. Phys. Soc. Sect. B. 64 (1951) 747–753. https://doi.org/10.1088/0370-1301/64/9/303.

[47] Iza-Mendia, A., and I. Gutiérrez. "Generalization of the existing relations between microstructure and yield stress from ferrite–pearlite to high strength steels." Materials Science and Engineering: A 561 (2013): 40-51.

[48] L.P. Kubin, A. Mortensen, Geometrically necessary dislocations and strain-gradient plasticity: A few critical issues, Scr. Mater. 48 (2003) 119–125. https://doi.org/10.1016/S1359-6462(02)00335-4.

[49] N. Isasti, D. Jorge-Badiola, J. Alkorta, P. Uranga, Analysis of Complex Steel Microstructures by High-Resolution EBSD, Jom. 68 (2016) 215–223. https://doi.org/10.1007/s11837-015-1677-0.

[50] M.F. Ashby, Strengthening methods in crystals, London, UK, 1971. https://doi.org/10.1016/0010-4361(71)90158-3.

[51] S.K. Paul, Non-linear correlation between uniaxial tensile properties and shear-edge hole expansion ratio, J. Mater. Eng. Perform. 23 (2014) 3610–3619. https://doi.org/10.1007/s11665-014-1161-y.

[52] J.I. Yoon, J. Jung, H.H. Lee, G.-S. Kim, H.S. Kim, Factors governing hole expansion ratio of steel sheets with smooth sheared edge, Met. Mater. Int. 22 (2016) 1009–1014. https://doi.org/10.1007/s12540-016-6346-5.

[53] K. Hasegawa, K. Kawamura, T. Urabe, Y. Hosoya, Effects of microstructure on stretch-flange-formability of 980 MPa grade cold-rolled ultra high strength steel sheets, ISIJ Int. 44 (2004) 603–609. https://doi.org/10.2355/isijinternational.44.603.

[54] B.S. Levy, M. Gibbs, C.J. Van Tyne, Failure during sheared edge stretching of dual-phase steels, Metall. Mater. Trans. A. 44 (2013) 3635–3648. https://doi.org/10.1007/s11661-013-1718-7.

[55] N. Pathak, C. Butcher, M. Worswick, E. Bellhouse, J. Gao, Damage evolution in complex-phase and dual-phase steels during edge stretching, Materials (Basel). 10 (2017) 346. https://doi.org/10.3390/ma10040346.